Reliability Assessment of Actuator Architectures for Unmanned Aircraft

A THESIS
SUBMITTED TO THE FACULTY OF THE GRADUATE SCHOOL
OF THE UNIVERSITY OF MINNESOTA
BY

Raghu Venkataraman

IN PARTIAL FULFILLMENT OF THE REQUIREMENTS
FOR THE DEGREE OF
MASTER OF SCIENCE

Peter Seiler, advisor

May, 2015

Acknowledgements

I am grateful to my family for having supported every one of my academic endeavors. I am especially grateful for their support of my graduate education in the United States.

I want to thank everyone who has been around me in graduate school. Specifically, thanks to Dr. Peter Seiler for his guidance, encouragement, and patience throughout my education and research at Minnesota. I am grateful to have an advisor like him. Many thanks to Dr. Demoz Gebre-Egziabher for his guidance and support, both in the classroom and in research.

I want to thank the several excellent teachers I have had in Minnesota, including Dr. Sairaj Dhople, Dr. Mihailo Jovanovic, and Dr. Yohannes Ketema. Thanks to Brian Taylor and Chris Regan at the Unmanned Aerial Vehicle Laboratory for developing and maintaining a world-class experimental flight research facility. Special thanks goes to Dr. Bálint Vanek and Márk Lukátsi at the Institute for Computer Science and Control, Hungarian Academy of Sciences (SZTAKI).

Many thanks to every one of my colleagues who has been around in graduate school.

Finally, I am thankful to the sponsors of this research. This work was supported by the National Science Foundation under Grant No. NSF/CNS-1329390 entitled ”CPS: Breakthrough: Collaborative Research: Managing Uncertainty in the Design of Safety-Critical Aviation Systems”. Any opinions, findings, and conclusions expressed in this thesis are those of the author and do not necessarily reflect the views of the National Science Foundation.

Dedication

To my family for always supporting my endeavors.

Abstract

Regulatory agencies worldwide are working towards safely integrating unmanned aircraft into their respective national airspaces. Reliability assessment of unmanned aircraft is a key step in the certification process. This thesis presents an analysis framework for the reliability assessment of small unmanned aircraft. Specifically, the effect of the placement of actuators and control surfaces on the overall aircraft reliability is investigated. The analysis framework is applied to several candidate actuator architectures of an example small unmanned aircraft. The candidate architectures have different numbers of controllable surfaces and servos. It is assumed that a servo fault detection algorithm is available and affected by known rates of false alarms and missed detections. The flight envelope of the aircraft is analyzed to determine the fault magnitudes for which the aircraft can still be flown around a feasible trim point. For these *allowable* fault magnitudes, it is assumed that the flight control law can be suitably reconfigured such that a safe landing is possible. Finally, the probability of catastrophic failure of the aircraft is estimated. In applying the framework to assess the reliability of the candidate architectures, several interesting and non-intuitive observations are made. These observations, and their resulting conclusions, have implications for the unmanned aircraft design process. Thus, in addition to being used for analysis, the proposed framework provides some insight into how reliability fits into the traditional aircraft design process.

Contents

List of Tables

List of Figures

Chapter 1

Introduction

The small Unmanned Aerial Vehicle/System (UAV/UAS) industry is undergoing a rapid transformation due to the emergence of several commercial applications, such as law enforcement, search & rescue, and precision agriculture. The commercial UAV market is projected to surpass the military market in the coming years [1]. Despite these indicators, widespread commercial use of UAVs is still at least one decade away. A barrier for UAS commercialization is their (current) inability to safely and reliably access common airspace. This is due to a combination of regulatory and technical challenges. On the regulatory side, significant work is currently underway, both in the United States (US) and in the European Union (EU), to establish a long-term framework for the seamless integration of UAVs into their respective national airspaces. On the technical side, challenges such as sense & avoid capabilities, secure communication, human factors considerations, etc need to be addressed.

1.1 Integration of UAVs into the National Airspace

It is predicted that 7,500 small UAVs (weighing 55 pounds or less) will be operating in the US by 2018. In addition to the US, there is strong interest from agriculture, mining, and infrastructure companies in using UAVs in Europe [2]. While UASs are projected to operate increasingly in airspace typically reserved for manned aircraft, their current reliability metrics do not meet the certification standards set by the Federal Aviation Administration (FAA) for manned aircraft. In 2012, the United States Congress passed

H.R.658 [3] - the FAA Modernization and Reform Act - in order to facilitate the safe integration of UASs into the national airspace. In particular, section 332 of H.R.658 mandates the FAA to "provide for the safe integration of civil unmanned aircraft systems into the national airspace system as soon as practicable, but not later than September 30, 2015."

More recently, the FAA released a Notice of Proposed Rulemaking (NPRM) [4] that specifies aircraft requirements and their operational limitations in US skies. The NPRM serves as a starting point for the detailed certification standards for UAVs that the FAA is expected to release in the future.

1.2 Reliability of Unmanned Aircraft

To understand the challenges of integrating UAVs into the national airspace, consider the current safety standards set by the FAA for manned commercial aircraft. In order for a commercial aircraft to be certified, there should be no more than one catastrophic failure per one billion hours of flight operation. Airframe manufacturers, such as Boeing, meet the 10^{-9} failures-per-flight-hour standard by utilizing hardware redundancy in their designs. For example, the Boeing 777 has 14 spoilers each with its own actuator; two actuators each for the outboard ailerons, left & right elevators, and flaperons; and three actuators for the single rudder [5]. In addition, the computing platform, electrical and hydraulic power lines, and communication paths have triple layer redundancy.

On the other hand, most civil UASs have reliabilities that are orders of magnitude below the 10^{-9} level required for manned commercial aircraft. For instance, the UAV Research Group at the University of Minnesota (UMN) [6] operates an *Ultra Stick 120* aircraft (described further in section 2) with single-string, off-the-shelf components. A comprehensive fault tree analysis yielded a failure rate of 2.2×10^{-2} failures-per-flight-hour [1] for this aircraft [7]. UASs have such low reliability because most, if not all, of their on-board components are single-string, i.e. there are single points of failure on the UAS that can lead to a system-level catastrophic failure.

The standard solution to increasing the reliability of aircraft is adding hardware

---

[1] This analysis provides a theoretical estimate of the reliability and no loss of aircraft has occurred to date.

redundancy, as seen with the example of the Boeing 777. Such an approach is not feasible for small UAVs due to the costs associated with size, weight, and power. Adding multiple copies of components that perform the same function is not economical for small UAVs that have limited payload and small margins on the design parameters. Cross-functional hardware redundancy offers a better approach to increased reliability of UAVs. Cross-functional components perform two or more functions and, thus, add more reliability value for a unit increase in the size and weight of the system. As an example, consider ailerons that are no longer constrained to deflect anti-symmetrically. Removing this constraint effectively turns ailerons into elevons. Elevons are cross-functional because they can provide both pitch and roll control authorities. Such cross-functionality in the flight dynamics is illustrated in this thesis.

1.3 Reliability Assessment of UAVs

One of the technical challenges, for the safe integration of UAVs, is increasing their reliability. While increasing the reliability is important, it is equally important to be able to quantify these increases. Reliability quantification is important to be able to close the loop and prove compliance with certification standards. Reliability assessment is a vast and well-studied field [8, 9]. The aerospace industry heavily relies on tools such as fault tree analysis and failure modes & effects analysis for the reliability assessment of aircraft and spacecraft. These assessment methodologies have typically treated faults as binary causes that lead to binary effects. However, fault causes and their effects are often better quantified probabilistically. While such a probabilistic treatment of faults is not new, the real challenge lies in connecting the reliability of individual components or subsystems to the overall system reliability. This thesis provides a framework, under certain assumptions, to connect the reliability of actuator servos (component) to that of the aircraft (system).

The overall system reliability of an aircraft is usually decomposed into component-level reliability by using a fault tree. The reliability of individual servo motors as well as the placement of aerodynamic control surfaces are usually the leaves of the fault tree. The phrase *actuator architecture* is used to describe the placement of control surfaces and how they are connected to the servo motors. The actuator architecture of an aircraft affects its flight envelope, i.e. boundaries in the state-space for safe flight. The flight envelope of an aircraft can be shown to be related to its overall reliability. By optimally choosing the aircraft's actuator architecture, the flight envelope can be modified in such a way that the overall reliability is maximized. Thus, the problem of choosing the optimal actuator architecture is both a design and an analysis problem. The scope of this thesis is limited to the reliability assessment of actuator architectures. A general framework is presented for such analyses.

In addition to being used as a reliability analysis tool, the framework can help understand the design trade-offs inherent in systems engineering. One of the trade-offs that is explored is between reliability and number of redundant components. The framework is presented for the stuck control surface fault mode, although it can be extended to cover other fault modes as well. A case study is presented to illustrate the use of the framework in assessing the reliability of several candidate actuator architectures. The candidate actuator architectures that are presented in this thesis are different in the extent to which they exploit cross-functionality in the aerodynamic control surfaces. This, in turn, affects the flight envelopes and overall reliability of the architectures.

The following chapters in this thesis contain the problem formulation and the general framework, and illustrate the framework on a case study. Several simplifying assumptions are made along the way in order to make the analysis tractable. Traditional aircraft reliability methods model the effects of the fault as a binary process: a fault, if present, will lead to a catastrophic failure. This research introduces a probabilistic notion to faults. In doing so, some credit is given to the fact that some failure modes can be tolerated (with sub-par performance), but do not necessarily lead to catastrophic failure.

Chapter 2

Problem Formulation

2.1 Catastrophic Failure

The reliability of an aircraft is typically quantified via the probability of catastrophic failure. This is a key metric, based on which commercial aircraft are certified for operation (see section 1.2). For the work presented in this thesis, catastrophic failure is considered as situations where irrecoverable loss of control occurs. Under such loss of control, the UAV will be unable to safely reach a proper landing site. Catastrophic failures have several causes, such as actuator failure, sensor failure, structural damage, weather-related phenomena, etc. Reliability analysis tools such as fault trees and failure modes & effects analysis help understand the relationship between the (low-level) causes and (high-level) effects.

2.2 Actuator Failure

This thesis will focus only on actuator failures. Actuators contain a lot of moving parts and are amongst the least reliable components on a UAV. Since actuators are connected to aerodynamic control surfaces, actuator faults directly affect the flight dynamics of the UAV. Many small UAVs use hobby-grade servo motors, which have failure times on the order of thousands of hours. Actuator failures can lead to significant loss in controllability of the aircraft and, eventually, catastrophic failure. It may be possible, in some cases, to adequately compensate for actuator failures by utilizing other actuators that may be present on the aircraft. Reconfiguration of control surface faults involves aspects of flight dynamics and these are covered in chapter 4.

Actuators can fail in several different modes, such as getting stuck in a position, losing efficiency, oscillating [10], etc. Loss in efficiency and oscillatory failures are more common in large aircraft where large loads are present and are less common in small UAVs. This thesis will only consider stuck actuator faults and analyze the impact on the overall system. Servo reliability will be represented by the metric *mean time between failures* (MTBF). The motor-propeller pair on a UAV can also be considered as an actuator. However, motor failure is not considered in this thesis. It is assumed that, under a motor failure, the aircraft can glide to a safe landing.

After an actuator fails, a path needs to be generated to a safe landing site. This flight path can be assumed to be composed of canonical paths such as: straight & level, banked turns, ascents, and descents. In order for the UAV to safely fly to a landing site, it must be capable of executing at least some of these canonical maneuvers. The minimum set of canonical maneuvers can be translated into a minimal flight envelope in the flight path angle - heading rate plane. This minimal flight envelope is explained in detail in section 4.

2.3 Reliability Analysis Framework

The analysis framework can be used to assess the reliability of UAV actuator architectures. In this thesis, the analysis framework is presented and simultaneously applied to a case study. The case study and the UAV platform therein are explained in section 2.5. This section briefly explains the components of the framework. Given a UAV and a specific actuator architecture, the analysis method is applied in a sequence of three consecutive steps. These are as follows.

- Determine the probability distributions of the control surfaces.
- Determine the flight envelope of the UAV under failures of different actuators.
- Estimate the probability of catastrophic failure, after actuator failures have occurred.

Given a mission and a UAV actuator architecture, the deflections of the control surfaces can be logged through simulation or flight measurements. Subsequently, histograms of the control surface deflections can be generated. In parallel, flight envelope assessment can be used to determine the flight characteristics after a fault has occurred. Specifically, under an actuator fault, the maneuvers that an aircraft can perform can be determined. With these two pieces of information, the probability of catastrophic failure can be estimated.

Each of these three steps have a chapter dedicated to their details. The steps are best illustrated immediately after they are introduced. The next section describes the UAV platform used for the case study and the candidate actuator architectures chosen for the illustration.

2.4 Infrastructure

The framework is applied to a small UAV called BALDR. BALDR is maintained and operated by the Unmanned Aerial Vehicle Laboratory at the University of Minnesota [6]. The airframe is a commercial, off-the-shelf, radio-controlled aircraft called the Ultra Stick 120 [11], shown in figure 2.1. The Ultra Stick 120 has a wingspan of 1.92 m and a mass of about 7.4 kg. The UMN UAV Research Group has retrofitted the airframe with custom avionics [6, 12, 13] for enabling research in the areas of real-time control, guidance, navigation, and fault detection. The avionics include a sensor suite, a flight control computer, and a telemetry radio. The airframe comes equipped with the standard suite of aerodynamic control surfaces - flaps, ailerons, elevator, and rudder - each actuated by its own servo motor.

A comprehensive reliability analysis was performed to identify the critical components on the Ultra Stick 120 [7]. In particular, two standard reliability analyses were performed: fault tree analysis (FTA) and failure modes & effects analysis (FMEA). These analyses identified the most critical components on the aircraft that should be supplemented with hardware redundancy. Through simulation, it was concluded that a stuck rudder and/or a stuck elevator would result either in a loss of mission (LOM) or loss of aircraft (LOA) depending on the fault level, airspeed, and altitude. In order to mitigate the degradation in performance during LOM and prevent LOA, the airframe

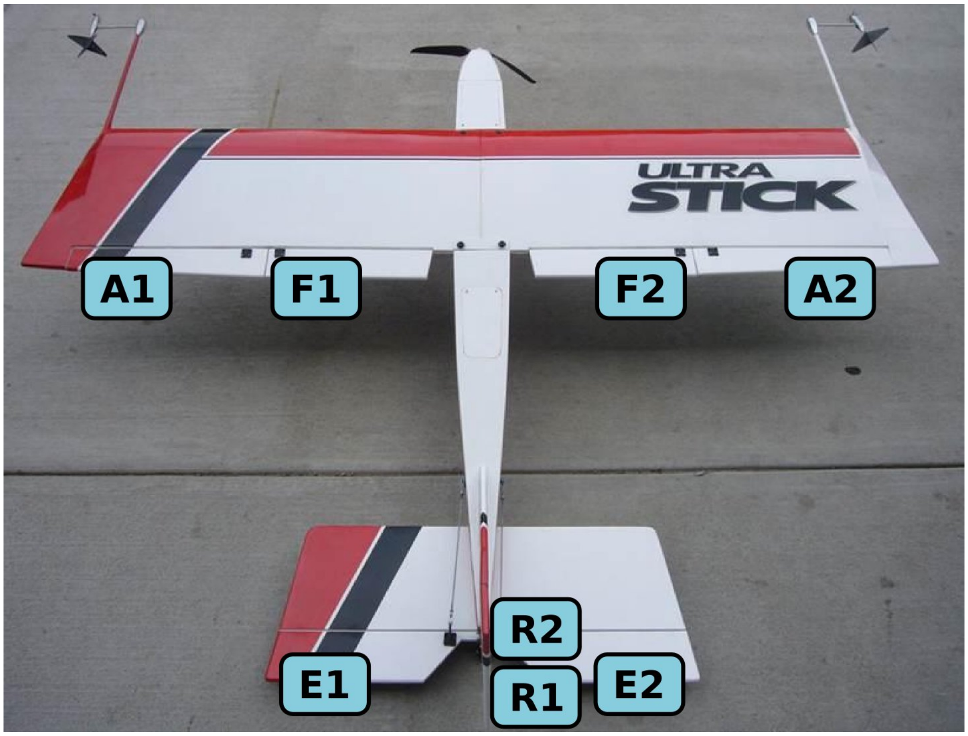

Figure 2.1: The BALDR UAV with the control surfaces labeled (A – aileron, F – flap, E – elevator, R – rudder).

was modified by splitting the rudder and elevator into two parts, each actuated by its own servo motor [14]. It was reasoned that if one of the two rudders got stuck in flight, the other rudder would be able to provide some limited yaw control authority, thereby allowing for the reconfiguration of the surfaces and effectively increasing the reliability of the airframe. A similar reasoning can be made for the split elevator. The split rudder is shown in Figure 2.2. The rudder was split in such a way that the top and bottom pieces have equal side force and yawing moment derivatives.

Including the split tail surfaces, this aircraft has a total of eight aerodynamic control surfaces. While each surface is independently actuated, the flight software allows for them to be coupled symmetrically (such as the elevators) or anti-symmetrically (such as the ailerons). In addition, these redundant surfaces allow for the testing and validation of reconfigurable control laws after a fault has been detected in the surfaces. From

Figure 2.2: Tail of the BALDR UAV with the control surfaces labeled (E – elevator, R – rudder).

an infrastructure standpoint, this aircraft serves as the test platform for all the safety-critical reliability research that is being undertaken by the UMN UAV Research Group.

The UMN UAV Research Group has developed a high-fidelity simulation environment for the Ultra Stick 120 with extensive documentation [6]. This simulation environment was built using Matlab/Simulink and contains models for the aircraft subsystems. The rigid body dynamics are implemented using the standard six degree-of-freedom, nonlinear aircraft equations of motion [15]. The aerodynamic stability and control derivatives were identified from wind tunnel experiments [16, 17]. The simulation models the forces & moments and the propwash generated by the electric motor and propeller pair. The simulation also includes first-order, rate and position limited actuator models for the servo motors. The sensor models for the inertial measurement unit, air data probes, and magnetometer include band-limited white noise for each measurement. The simulation environment also contains subsystems that model environmental effects, such as wind gusts, atmospheric turbulence, and the Earth's gravitational & magnetic fields. In particular, the Discrete Wind Gust Model and the Discrete Dryden Wind Turbulence

Model are added from Matlab's Aerospace Blockset. Finally, closed-loop flight control laws and navigation & guidance filters are also included.

The nonlinear aircraft model can be trimmed and linearized at any flight condition within the flight envelope of the aircraft. The simulation environment and the flight control computer allow for extensive software-in-the-loop and hardware-in-the-loop simulations of the aircraft model. The entire simulation environment, details about the aircraft fleet, components, wiring, and data from numerous flight tests have been made open-source and can be freely downloaded from the website of the UMN UAV research group [6].

2.5 Case Study

The BALDR UAV has eight unique aerodynamic control surfaces, as shown in figures 2.1 and 2.2. These are: split elevators ($E1, E2$), split rudders ($R1, R2$), ailerons ($A1, A2$), and flaps ($F1, F2$). Each of the eight surfaces is actuated by an independent servo motor. The BALDR UAV can be thought of a superset from which different reduced order actuator architectures can be generated, depending on whether the surfaces are coupled or free. The sign convention of the control surfaces is as follows. A trailing edge down deflection of the elevators, ailerons, and flaps is considered positive. A trailing edge left deflection of the rudders is considered positive. In addition, all the surfaces have a deflection range of $[-25^\circ, +25^\circ]$.

Increasing the number of servos on an aircraft increases reliability, if the architecture is properly designed. However, it often adds to the cost and weight. This trade-off can be analyzed by considering different actuator architectures. These actuator architectures are mainly defined by two parameters: the total number of servos and the coupling between various control surfaces. The actuator architectures are listed tabularly in table 2.1 and depicted pictorially in figure 2.3.

The configurations v0, . . . , v4 were chosen because they are representative of the most common actuator architectures found in small UAVs. As an example, consider the presence/absence of flaps across the five configurations. Flaps are not very common in small UAVs since they perform a very specific function and are not used for the majority of the flight duration. Since flaps are atypical, four configurations (v1 to v4) are not

Table 2.1: Actuator architectures listed tabularly.

Config.	Ailerons	Elevators	Rudders	Flaps	No. of servos
v0	Coupled	Coupled	Coupled	Coupled	4
v1	Decoupled	Coupled	Coupled	None	4
v2	Coupled	Decoupled	Coupled	None	4
v3	Coupled	Coupled	Coupled	None	3
v4	Decoupled	Coupled	None	None	3

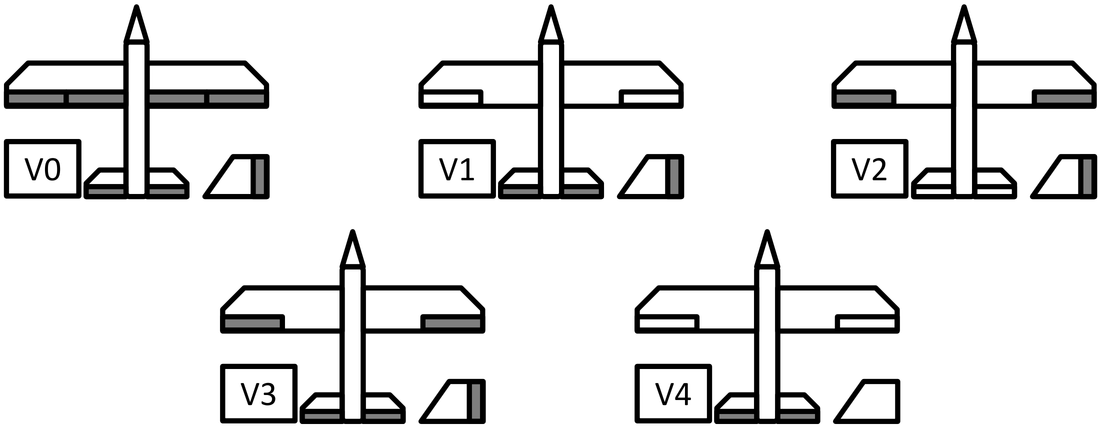

Figure 2.3: Actuator architectures depicted pictorially.

equipped with flaps. The only configuration that is equipped with flaps is v0. This is because v0 is only used for flight envelope assessment in section 4. On the other hand, all configurations have elevators and ailerons since these are required control surfaces. The eight different control surfaces of the BALDR are coupled differently depending on the actuator configuration. As an example, for the v0 configuration, $A1 = -A2$, $E1 = E2$, $R1 = R2$, and $F1 = F2$.

The five configurations cover different combinations of pitch & roll control authorities. For example, elevators, when decoupled, contribute to both pitching and rolling. The configurations are representative of small UAV architectures because they were chosen by balancing the need to maximize the pitch and roll control authorities against the need to minimize the number of servos. For example, an architecture that has decoupled elevators and decoupled ailerons is not considered. This is because, while such an architecture will exhibit higher reliability than any other, it would also require the use of many servos. In choosing the five configurations, it was ensured that the number of servos was at most equal to four. It should be noted that the BALDR UAV has many more control surfaces than will be found on a typical small UAV.

Several assumptions are made to make the analysis tractable. First, it is assumed that a fault detection and isolation (FDI) algorithm is used to detect actuator faults. The FDI algorithm could either be built-in tests [18] (self-diagnostics within actuators) or centralized monitoring systems [19]. For simplicity, only statistical properties, such as missed detection and false alarm rates, are considered. Second, it is assumed that if the aircraft is trimmable after a fault has occurred, an appropriate reconfigurable control law is available. In other words, transitions between trim points are without loss of control. Finally, it is assumed that multiple faults occur with negligible probabilities.

The next chapter describes the first step of the analysis, i.e. distributions of control surfaces.

Chapter 3

Distribution of Control Surfaces

3.1 Introduction

The first step in the analysis is determining the distribution of the aircraft's control surfaces. After performing a given mission, flight data logs will show the time history of deflection of each control surface. These time histories can be plotted as histograms. The distributions are influenced by several factors such as: mission profile, control law, exogenous disturbances (sensor noise, wind gusts, & turbulence), etc. Control laws significantly affect the distributions and, thereby, the overall reliability. As an example, the rudder will have different distributions depending on whether the control law is tuned for coordinated turns or yaw rate damping. More generally, the gains of the control law affect the shape of the distributions. The shape of the distributions, in turn, affect the overall reliability. By properly tuning the control law, the shape of the distributions can be tailored to meet performance as well as reliability requirements.

3.2 Characterization of Probability Distributions

Histograms of control surface deflections can be plotted from flight data or simulations. Subsequently, probability density functions can be estimated for these histograms. This approach is good when flight data is readily available. Presumably, flight data may not always be available for arbitrary mission profiles. For such scenarios, a more analytical approach can be followed, wherein the mission profile is decomposed into a number of

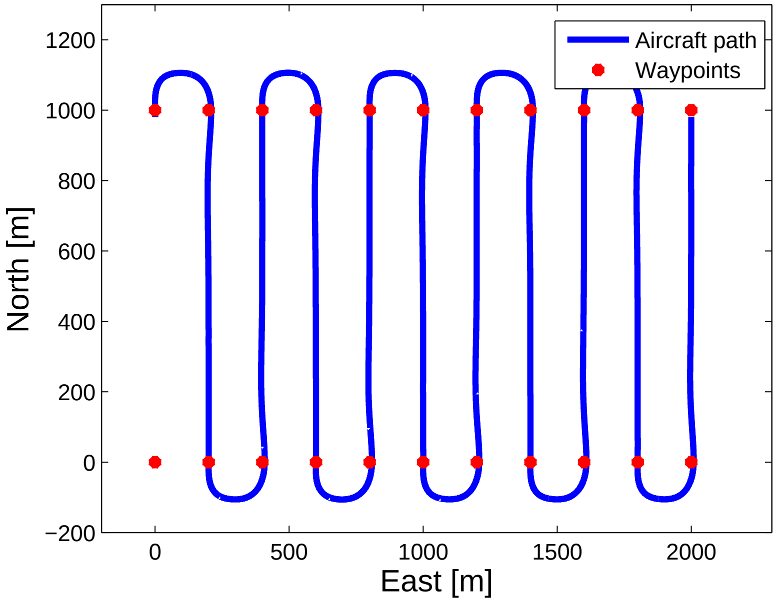

Figure 3.1: Aircraft path during area scanning mission.

flight modes. Flight modes are canonical maneuvers such as straight & level, turning, ascending, and descending flights. If the control surface distributions are known for these flight modes, the overall distributions can be constructed by combining them as a weighted sum, as shown in equation 3.1.

$$p_i(\delta) = \sum_{j=1}^{n} p_i(\delta|mode = j)p(mode = j), \tag{3.1}$$

where $p_i(\delta|mode = j)$ is the probability density function (PDF) of the ith control surface for mode j, and $p(mode = j)$ is the probability of occurrence of mode j. In this analytical approach, only a small library of PDFs need to be stored in order to be able to generate PDFs for arbitrary mission profiles.

Figure 3.1 shows a typical area scanning path for the BALDR UAV. The simulation duration is 588s. It consists of three flight modes: straight & level, left, and right banked turns. The probability of being in each mode is estimated from the mission profile as the fraction of time spent in that mode. For the area scanning mission, the probabilities of the modes can be calculated from the geometry of the flight path. For

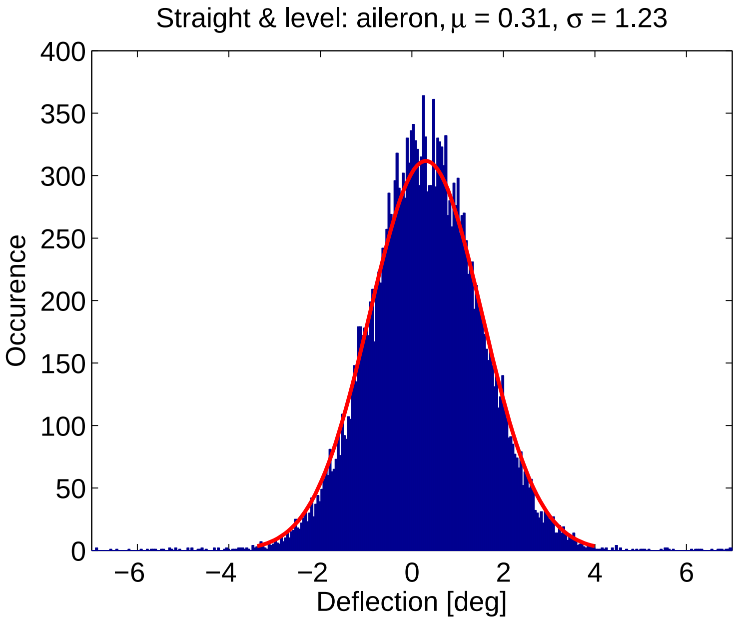

Figure 3.2: Aileron distribution for straight & level flight.

the path shown in figure 3.1, the waypoints are 1000m and 200m apart in the North and East directions, respectively. The resulting probabilities are 0.13 for both left and right turns and 0.74 for straight flight. In the reliability assessment presented in section 5, the histograms are used directly.

3.3 Histograms from data

Figures 3.2, 3.3, and 3.4 show the histograms of the deflections of the aileron, elevator, and rudder for straight & level flight. Similarly, figures 3.5, 3.6, and 3.7 show the histograms of the deflections of the aileron, elevator, and rudder for right banked turns. All figures correspond to the mission profile shown in figure 3.1. Normal distributions are fitted to the histograms of the ailerons and elevators because they are approximately Gaussian. (The mean and standard deviation of the distribution are denoted by μ and σ, respectively.) On the other hand, rudder distributions appear to be multi-modal and cannot be characterized easily. It is likely that rudder distributions can be fit using a

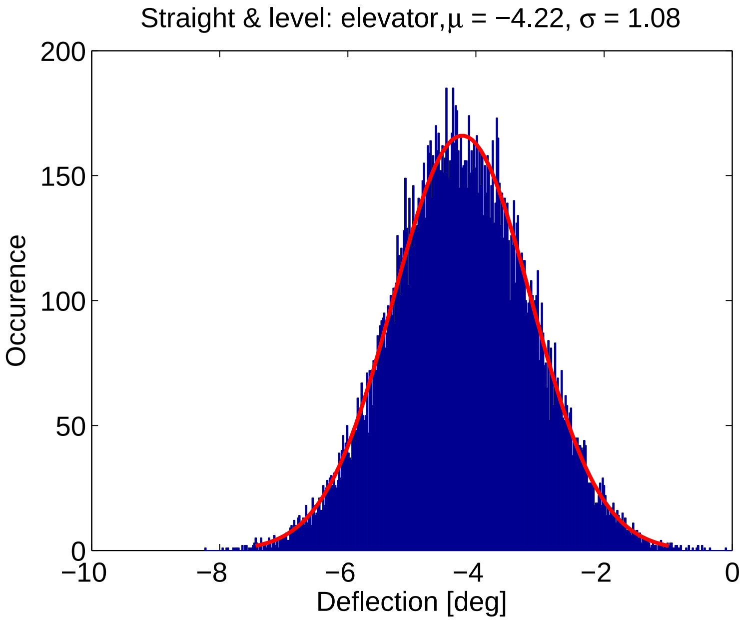

Figure 3.3: Elevator distribution for straight & level flight.

basis of Gaussian distributions. The underlying Gaussian nature of all these distributions is not surprising since these are simulated results. The simulation environment that was introduced in section 2.4 contains models for sensor noise and atmospheric turbulence. Both types of disturbances are fed by filtered Gaussian generators.

In addition to the aircraft dynamics, the controller dynamics also plays a role in shaping these distributions. As mentioned previously, the controller parameters offer a means for the control designer to shape these distribution functions. By shaping these distribution functions, performance and reliability requirements can be satisfied. Although the underlying generators maybe independently and identically distributed (iid), the noise that is seen in the control surfaces are temporally correlated. This is because these signals pass through dynamics (effectively nonlinear filters). Significantly, the distributions that are shown in figures 3.2 through 3.7 are neither independently nor identically distributed.

From figure 3.2, it is seen that during straight and level flight, the aileron trim is close to zero degrees. There is, however, a small non-zero mean aileron deflection that is used to compensate for the motor torque. During right banked turns, the mean aileron

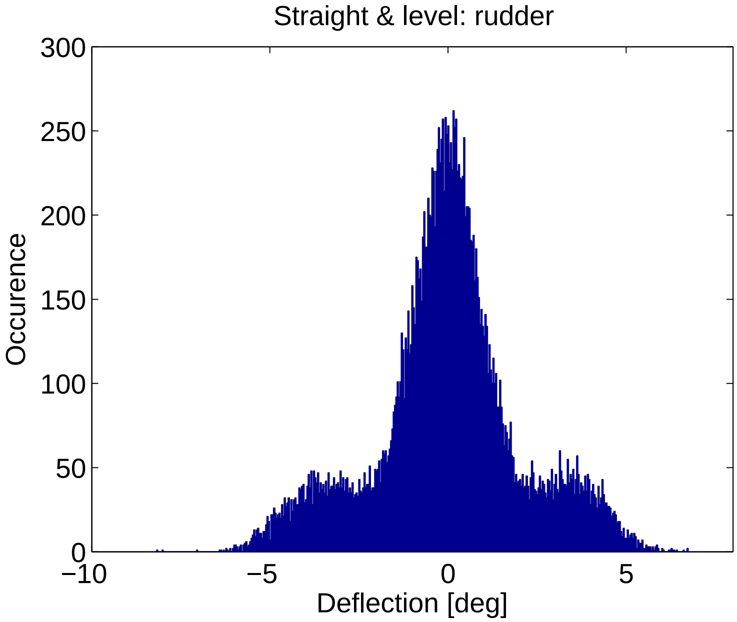

Figure 3.4: Rudder distribution for straight & level flight.

deflection is slightly larger at 1.04°, as shown in figure 3.5. This is because, ailerons are deflected only to change the bank angle of the aircraft and not to sustain turns. Once the desired bank angle has been reached, the ailerons return to their trim value and the aircraft enters into a steady banked turn.

From figure 3.3, it is seen that during straight and level flight, the elevator trim is $-4.22°$. This trim value corresponds to an angle of attack of approximately 5°. The distribution is fairly symmetric about the mean value. The mean and standard deviation of the elevator distribution are higher during banked turns, as seen in figure 3.6. This observation is also consistent with flight dynamics. For a given airspeed, the angle of attack increases during banked turns as compared to straight and level flight. Consequently, a larger elevator deflection (in magnitude) is necessary during banked turns. In both figures 3.3 and 3.6, the elevator range is approximately $[-10°, 0°]$.

From figure 3.4, it is seen that during straight and level flight, the rudder trim is close to zero degrees. In addition, the rudder distribution is symmetric about zero degrees, despite being multi-modal. Both these observations make physical sense. On the other hand, the rudder trim is non-zero during banked turns. Figure 3.7 shows

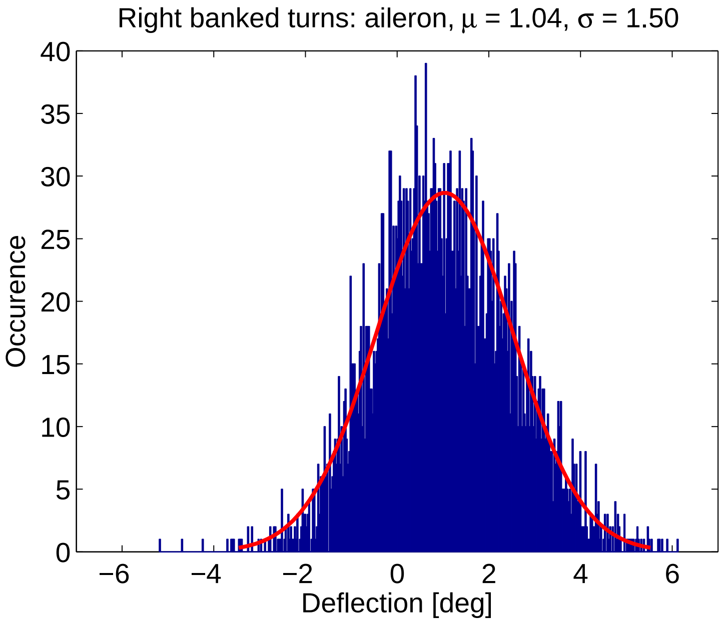

Figure 3.5: Aileron distribution for right banked turns.

a small negative trim value for the rudder during right banked turns. This difference exists because the control law used in these simulations deflects the rudder to maintain turn coordination. As right banked turns are being made, the trailing edge of the rudder is deflected rightward to maintain turn coordination. A rightward rudder deflection is negative, leading to the small negative mean.

Finally, it should be noted that the histograms only depend on the mission being executed and not on the actuator architecture. Before a fault occurs, all actuator architectures are controlled by the same baseline control law. This baseline control law actuates all surfaces as if they were coupled. In other words, the baseline control law is designed for architecture v0. It is only after a fault occurs that the actuator architecture matters for a successful reconfiguration.

In the next section, flight envelope assessment (the next step of the analysis) is introduced. The concept of flight envelopes is introduced followed by its application to BALDR.

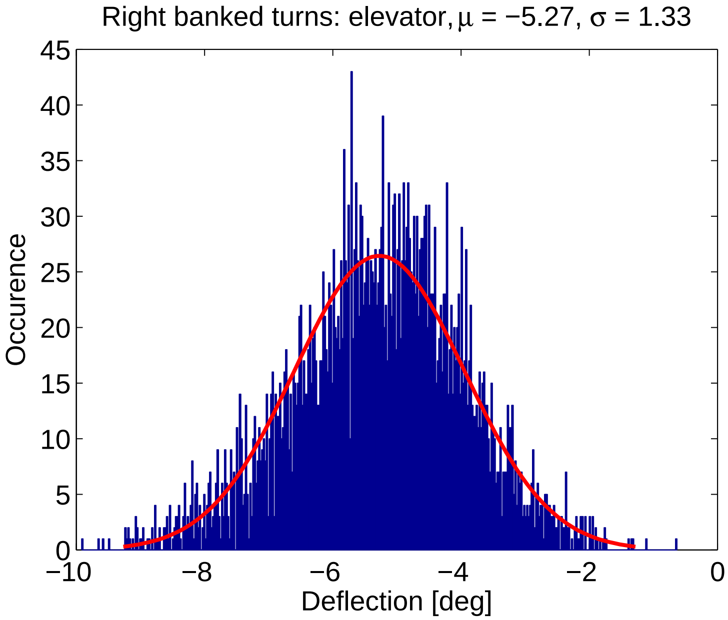

Figure 3.6: Elevator distribution for right banked turns.

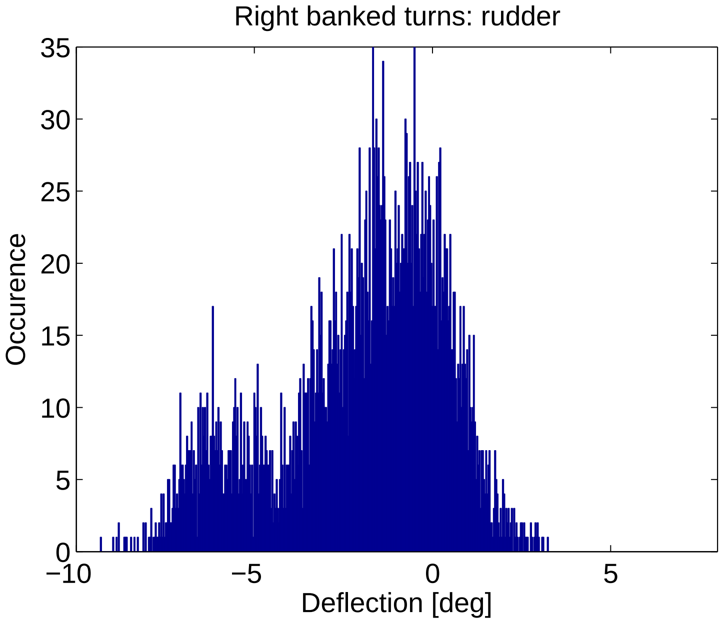

Figure 3.7: Rudder distribution for right banked turns.

Chapter 4

Flight Envelope Assessment

4.1 Introduction

This section gives a cursory introduction to aircraft flight envelopes, since this concept is important for the subsequent section. The aircraft equations of motion [20, 21] can be described in the nonlinear state-space form as shown in equations 4.1 and 4.2.

$$\dot{x} = f(x, u) \tag{4.1}$$

$$y = h(x, u) \tag{4.2}$$

In these equations, $x \in \mathbb{R}^n$ is the state vector, $u \in \mathbb{R}^m$ is the input vector, and $y \in \mathbb{R}^p$ is the output vector. In addition, $f : \mathbb{R}^n \times \mathbb{R}^m \to \mathbb{R}^n$ is the state function and $h : \mathbb{R}^n \times \mathbb{R}^m \to \mathbb{R}^p$ is the output function. The state vector is: $x = [\phi, \theta, \psi, p, q, r, u, v, w]^T$. Here, ϕ, θ, and ψ are the Euler angles of the aircraft. The aircraft's angular velocity components in the body-fixed frame are: roll rate (p), pitch rate (q), and yaw rate (r). The airspeed components in the body-fixed frame are u, v, and w. We also define a reduced order state vector that does not contain ψ: $x_r = [\phi, \theta, p, q, r, u, v, w]^T$. x_r is used in the definitions of the flight envelopes.

For configuration v0, there are only four unique aerodynamic inputs. In addition, the throttle for the motor is τ. Consequently, the input vector is $u = [\tau, E, R, A, F]$. As expected, the input vector will change appropriately, depending on the actuator configuration. The results presented in this chapter make use of certain elements in the output vector (y). The airspeed, angle of attack, and angle of sideslip are denoted by

V, α, and β, respectively. The flight path climb angle and heading rate are denoted by γ and $\dot{\psi}$, respectively.

Aircraft typically fly around equilibrium or trim points. These are operating points at which some state derivatives are zero, and others have constant values. The collection of all such trim points defines the steady flight envelope ($\mathbb{F}$) of the aircraft, as shown in equation 4.3.

$$\mathbb{F} = \{(\bar{x}, \bar{u}) : \dot{\bar{x}}_r = 0,\ \dot{\bar{u}} = 0\} \tag{4.3}$$

A subset of the flight envelope is straight and level flight, i.e. unaccelerated flight at constant altitude. This subset is mathematically described in equation 4.4. The key property of this subset is the zero flight path angle ($\bar{\gamma} = 0$).

$$\mathbb{F}_{straight,level} \quad = \quad \{(\bar{x}, \bar{u}) : f(\bar{x}, \bar{u}) = 0,\ \bar{p} = \bar{q} = \bar{r} = 0,\ \bar{\gamma} = 0,\ \dot{\bar{u}} = 0\} \tag{4.4}$$

Level flight is, by definition, at constant altitude. When the aircraft descends steadily, at a constant negative flight path angle ($\bar{\gamma} < 0$), the envelope is described by equation 4.5.

$$\mathbb{F}_{steady,descent} \quad = \quad \{(\bar{x}, \bar{u}) : f(\bar{x}, \bar{u}) = 0,\ \bar{p} = \bar{q} = \bar{r} = 0,\ \bar{\gamma} < 0,\ \dot{\bar{u}} = 0\} \tag{4.5}$$

Another subset of the flight envelope is steady banked turns at constant altitude. A steady banked turn is defined by a constant heading rate ($\dot{\psi}$). Left banked turns are described by a negative $\dot{\psi}$ and right banked turns are described by a positive $\dot{\psi}$. These subsets are mathematically defined in equations 4.6 and 4.7.

$$\mathbb{F}_{banked,left} = \{(\bar{x}, \bar{u}) : \dot{\bar{x}}_r = 0,\ \dot{\psi} < 0,\ \bar{\gamma} = 0,\ \dot{\bar{u}} = 0\} \tag{4.6}$$

$$\mathbb{F}_{banked,right} = \{(\bar{x}, \bar{u}) : \dot{\bar{x}}_r = 0,\ \dot{\psi} > 0,\ \bar{\gamma} = 0,\ \dot{\bar{u}} = 0\} \tag{4.7}$$

4.2 Computational Details

These subsets can be computed by applying numerical optimization techniques to the nonlinear aircraft model that was introduced in section 2. The nonlinear aircraft model can be trimmed and linearized, using routines developed in-house, at any operating point within the flight envelope. For straight & level flight, operating points are best expressed as pairs of (V, α). A rectangular grid of such (V, α) pairs is generated for

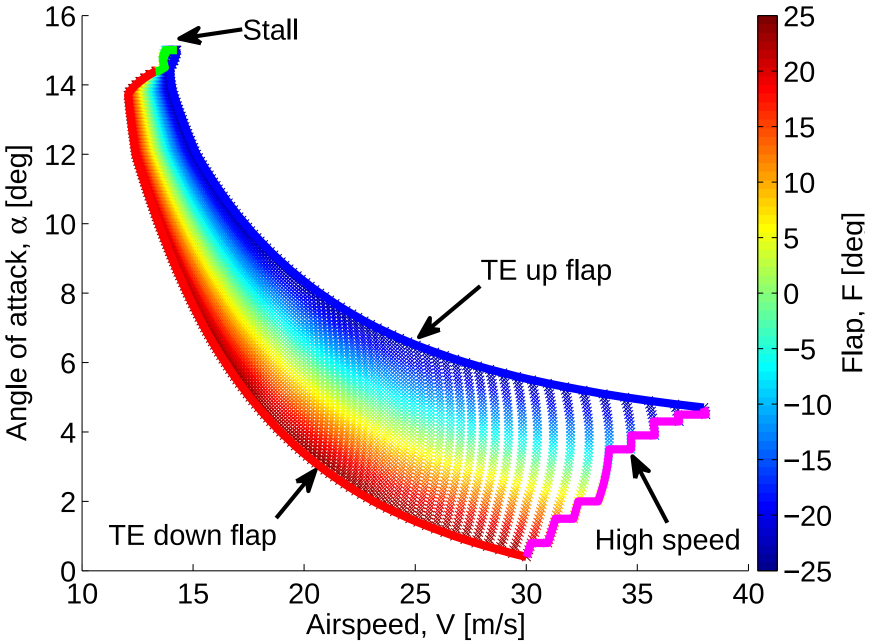

Figure 4.1: Longitudinal flight envelope in the $V \times \alpha$ plane.

$V \in [10, 40]\mathrm{m\,s^{-1}}$ and $\alpha \in [0°, 20°]$. The grid resolution is $0.1\mathrm{m\,s^{-1}}$ and $0.1°$ for V and α, respectively. The nominal flight condition for the BALDR is $(V, \alpha) = (23\mathrm{m\,s^{-1}}, 4.72°)$. The trim routine is called at each grid point after being initialized with the nominal flight condition. For a specific subset, the trim routine finds the minimum of a nonlinear, multi-variable cost function subject to the appropriate constraint (equations 4.4 – 4.7). Matlab's Optimization Toolbox contains the *fmincon* function that is well suited for this purpose. This optimization problem is non-convex and, in general, has multiple local minima. The *fmincon* function returns the minimum that is closest to the initial condition. A more thorough treatment of aircraft flight envelopes can be found in [22, 23, 24].

4.3 Flight Envelopes of BALDR

A limited flight envelope assessment is presented only for configuration v0. The envelope corresponding to longitudinal straight & level flight can be used to determine the stuck ranges for the elevator and flaps. This envelope is shown in the $V \times \alpha$ plane in figure 4.1

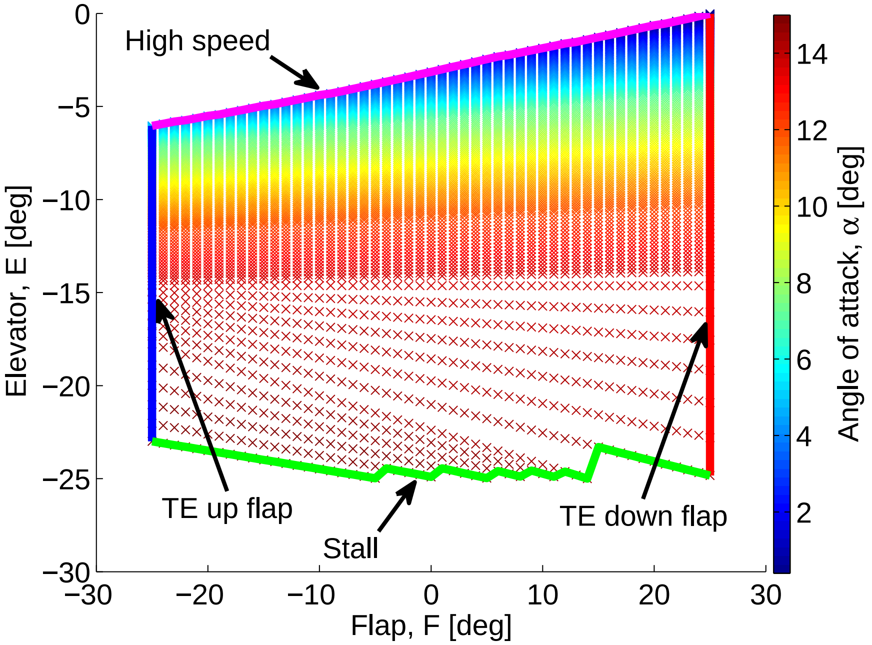

Figure 4.2: Longitudinal flight envelope in the $F \times E$ plane.

and in the $F \times E$ plane in figure 4.2. Trim points are marked by colored crosses in both these figures. In figure 4.1, the trim points are colored based on the value of the flap deflection. There are several interesting observations. First, as expected, there is an inverse relationship between V and α. Trim points at high airspeeds have low α and vice-versa. Second, since a nonlinear aircraft model is being trimmed, the inputs and outputs are implicitly constrained. As a result, the flight envelope has well-defined boundaries, as seen in figure 4.1.

The high speed boundary is a collection of trim points that define the highest achievable airspeeds and lowest achievable angles of attack. Conversely, at the stall boundary, the stall angle of attack (approximately 15°) is reached at low airspeeds. The high speed and stall boundaries are due to output constraints. The other two boundaries are due to input saturation. The TE up flap boundary defines trim points for which flaps are deflected to $-25°$ (trailing edge up). The TE down flap boundary defines trim points for which flaps are deflected to $+25°$ (trailing edge down). It is interesting to note that within these boundaries, fixed flap deflections define isolines that follow the general shape of the envelope. Although this envelope is plotted for configuration v0, the envelopes for other configurations can be extracted by looking at certain isolines. As an example, consider configuration v3, where no flaps are used. The flight envelope for this configuration would simply be the green isoline for $F = 0$ shown in figure 4.1.

In figure 4.2, the trim points are colored based on the value of α. Three important conclusions can be drawn from this figure. Firstly, it is seen that trim points exist for the entire range of flap deflections, as shown by the TE up/down flap boundaries. Secondly, there are no trim points for a positively deflected elevator. This implies that if the elevator was to get stuck positively, the result would be a catastrophic failure of the aircraft. As an example, for configuration v3 ($F = 0$), trim points exist for the elevator range $[-25°, -4°]$. It is seen that, for any given flap deflection, the high speed boundary is reached when the elevator is deflected to its highest trimmable value. Conversely, the stall boundary is reached for the lowest trimmable value of the elevator.

4.4 Minimal Flight Envelope

A stuck surface fault is called *allowable* if the aircraft can safely fly home in the presence of this fault. In order to safely fly home, the aircraft should be able to execute some limited maneuvers. The flight envelope subsets, that were defined earlier, can be used to describe these limited maneuvers. The aircraft should be able to fly straight and level, execute either left or right banked turns with some minimum $\dot{\psi}$, and descend steadily at some minimum γ. These limited maneuvers together form the minimal flight envelope. This can be visualized in the $\gamma - \dot{\psi}$ plane, as shown in figure 4.3. It is reasoned that as long as the actual flight envelope, in the presence of a stuck fault, is larger than this minimal flight envelope, the aircraft can safely fly home.

For this research, the maximum required turning radius is 87m. This value was selected because it is sufficiently larger than the minimum achievable turning radius of 54m, while still allowing for reasonably large heading rates. At a nominal airspeed of $V = 20\mathrm{m\,s}^{-1}$, an 87m turning radius corresponds to a heading rate of $\pm 13°/s$. The minimum required flight path angle is chosen as $\gamma = -3°$ since this is representative of typical glide slopes. The four points shown in figure 4.3 define two triangles: $\mathbb{F}_{minimal,left}$ and $\mathbb{F}_{minimal,right}$. Furthermore, it is assumed that if trim points exist at the vertices

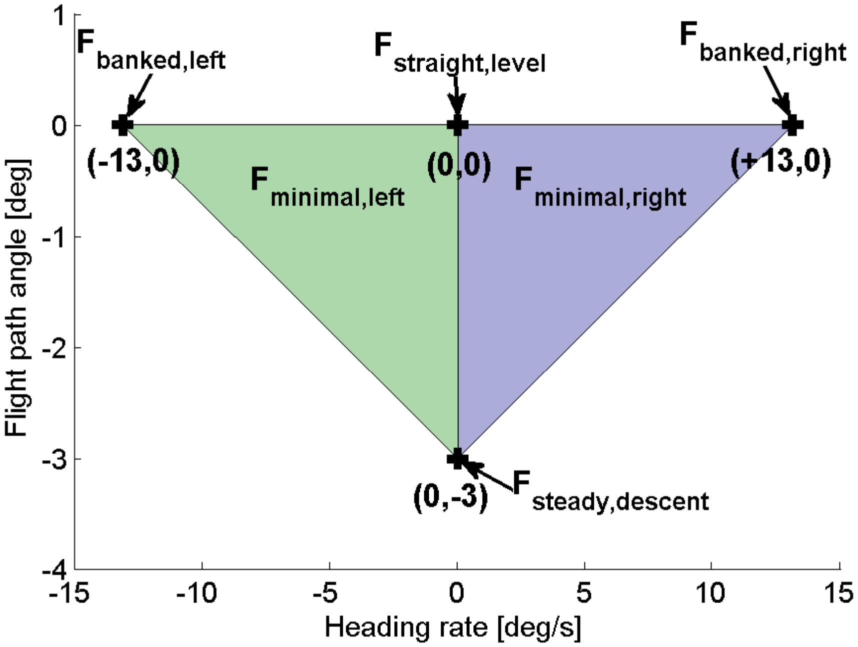

Figure 4.3: Minimal flight envelope

of either of these two triangles, trim points exist in all of the corresponding triangle. Hence, it is sufficient to check for the existence of trim points at the vertices of the two triangles.

For any given stuck fault, in order to safely fly home, at least one trim point needs to be found in each of the subsets $\mathbb{F}_{straight,level}$ and $\mathbb{F}_{steady,descent}$, and either of the subsets $\mathbb{F}_{banked,left}$ and $\mathbb{F}_{banked,right}$. In other words, a stuck fault is called allowable if trim points can be found either in $\mathbb{F}_{minimal,left}$ or $\mathbb{F}_{minimal,right}$. In checking for the existence of trim points, no explicit constraints (such as a zero sideslip angle requirement) are placed on V, α, and β.

4.5 Allowable Surface Faults

The following steps describe the calculation of the allowable stuck surface ranges. First, the trimmable range for each surface is calculated at each of the four points shown in figure 4.3. Then, the intersection of these trimmable ranges is calculated between

Table 4.1: Allowable stuck surface ranges.

Config.	Elevator(s)	Rudder(s)	Aileron(s)
v1	[-25,-1]	[-25,+25]	[-25,+25]
v2	[-25,+25]	[-25,+25]	[-11,+12]
v3	[-25,-4]	[-25,+25]	[-7,+10]
v4	[-25,-1]	N/A	[-25,+25]

$\mathbb{F}_{straight,level}$, $\mathbb{F}_{steady,descent}$, and $\mathbb{F}_{banked,left}$. This intersection is called the trimmable range for $\mathbb{F}_{minimal,left}$. In a similar way, the trimmable range for $\mathbb{F}_{minimal,right}$ is calculated. The union of $\mathbb{F}_{minimal,left}$ and $\mathbb{F}_{minimal,right}$ is defined as the allowable stuck surface range.

The allowable stuck surface ranges for v1 through v4 are given in table 4.1. For configurations that have a single elevator (v1, v3, v4), it is seen that the range is never positive, i.e. no trim points exist for positively stuck elevator. However, the allowable range is $[-25°, +25°]$ when split elevators are present (v2). Another interesting observation is that stuck rudder faults can always be tolerated as long as no explicit constraints are placed on β. Lastly, decoupled ailerons (v1 and v4) have the full allowable range as compared to coupled ailerons (v2 and v3). The allowable stuck surface ranges presented here in conjunction with the distribution of control signals, presented in section 3, allow for the computation of the probability of catastrophic failure for each of the four configurations. It is generally observed that cross-functionality in the aerodynamic control surfaces helps increase the overall reliability of the UAV.

The next chapter introduces the final step of the analysis method: computing the probability of catastrophic failure.

Chapter 5

Probability of Catastrophic Failure

5.1 Fault Tree Analysis

The final step of the analysis is computing the probability of catastrophic failure (P_{SYS}). Figure 5.1 shows a fault tree. The first level of the tree is the servo failure rate (q), which is the inverse of the mean time between failures (MTBF). The next level captures the positional probabilities of the control surfaces. The final level captures false alarm (P_{FA}) and missed detection (P_{MD}) rates. Events that lead to catastrophic failure are marked red and the others green. The probability of the ith surface being outside the allowable range $[l, u]$ is:

$$P_{out,i} = 1 - \int_l^u p_i(\delta_i) d\delta_i. \tag{5.1}$$

The probability of the ith surface getting stuck outside the allowable range is $qP_{out,i}$. Considering N control surfaces, the total probability of catastrophic failure is:

$$P_{SYS} = \sum_{i=1}^{N} qP_{out,i} + q(1 - P_{out,i})P_{MD} + (1 - q)P_{out,i}P_{FA}. \tag{5.2}$$

Missed detections lead to catastrophic failure, irrespective of the surface position. False alarms lead to catastrophic failure, but only outside the allowable range. It is assumed that faults inside the range can be tolerated.

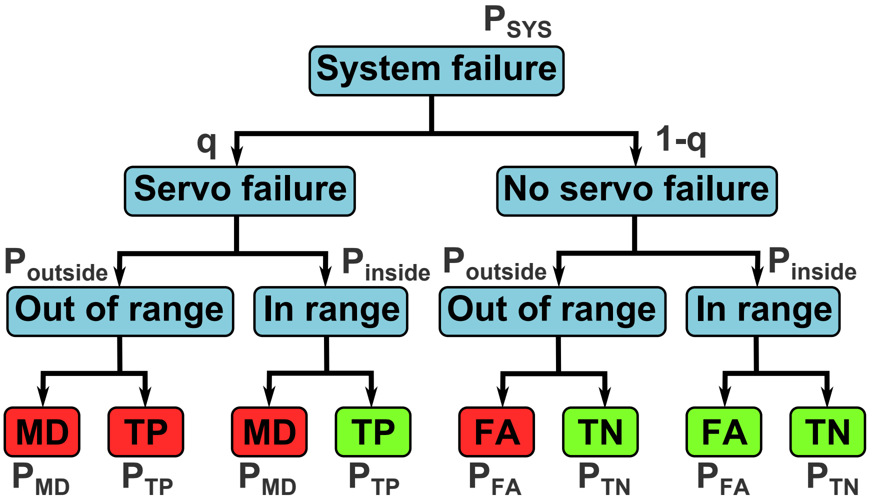

Figure 5.1: Fault tree (MD – missed detection, TP – true positive, FA – false alarm, TN – true negative).

5.2 Application to Candidate Architectures

The framework is applied to configurations v1, . . . , v4. Figure 5.2 shows the probabilities as a function of servo MTBF with $P_{MD} = 0.05$ and $P_{FA} = 0.01$. The servo MTBF range from common R/C-grade [25] to high performance [26]. For example, [27] servos have a high MTBF (1000 hours). Typical built-in tests cover more than 95% of faults [18]. Hence, $P_{MD} = 0.05$ in figure 5.2. It is assumed that current FDI algorithms allow for $P_{FA} = 0.01$.

From figure 5.2, the probability of failure for v3 is two orders of magnitude greater than that of the other architectures. This is because configuration v3 has no decoupled surfaces implying there is very little cross-functionality. v1 is the second-to-worst architecture, despite having 4 servos. Compared to v3, v1 has an extra servo that decouples the ailerons and extends their allowable range to $[-25°, +25°]$. This greatly increases the reliability of v1 relative to v3. However, v1 (4 servos) is less reliable than v4 (3 servos). This demonstrates that increasing the number of servos does not necessarily increase the reliability.

Finally, the two most reliable configurations are v2 (4 servos) and v4 (3 servos). For low servo MTBF, the probability of failure is lower for v4. On the other hand, for high

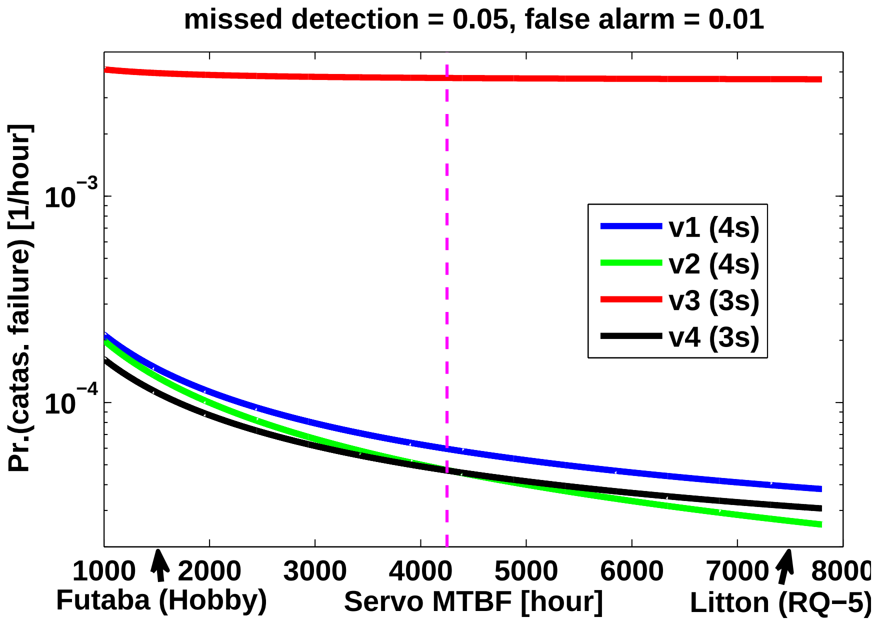

Figure 5.2: Probability of failure as a function of servo MTBF.

servo MTBF, the probability of failure is lower for v2. Excluding the rudder, both v2 and v4 use a three-servo architecture. While v2 has coupled ailerons and decoupled elevators, v4 has decoupled ailerons and coupled elevators. The presence/absence of the rudder in v2 and v4 is the reason for the total number of servos being different. However, table 4.1 indicates that rudder faults of any magnitude can be tolerated. Thus, the difference between v2 and v4 is primarily driven by the architecture of the elevators and ailerons. It is generally concluded that when low reliability servos are used, an architecture that decouples the ailerons (v4) is more reliable. On the other hand, when high reliability servos are used, an architecture that decouples the elevators (v2) is more reliable.

It would be naive to generalize this conclusion any further. The plots shown in figure 5.2 are functions of several variables such as: servo reliability, actuator placement, surface coupling, mission, etc. In general, there is a complex interplay between these different variables as shown by [28]. All the candidate architectures considered in this case study are single-string designs. Thus, the cross-functionality of the surfaces is a major contributor to the overall reliability of the UAVs. Increasing the cross-functionality

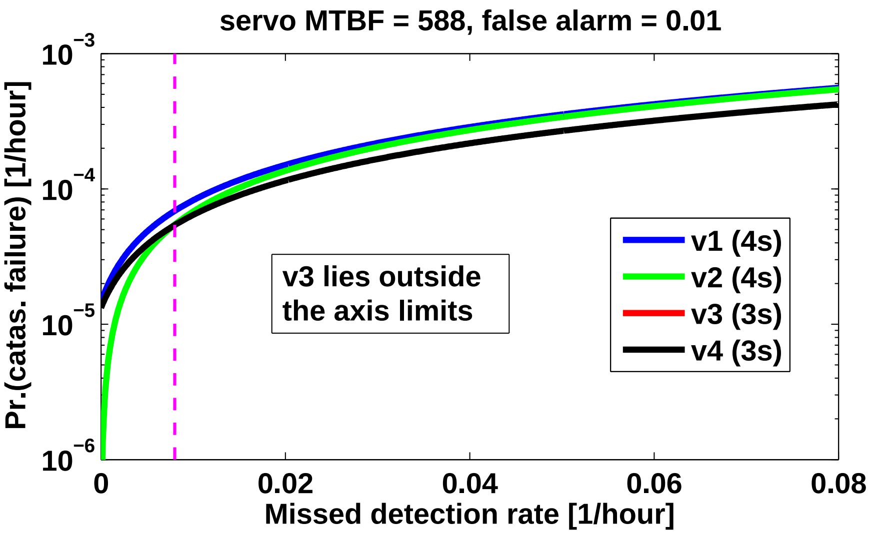

Figure 5.3: Probability of failure as a function of missed detection.

between surfaces can help increase the overall reliability with minimal increases in size and weight. Traditional reliability analyses do not take credit for the cross-functionality between components. By considering the flight envelope of the UAV, the framework presented is able to take credit for the cross-functionality between surfaces. In addition to the flight envelope assessment, modeling the stochastic nature of surface faults and connecting them to the mission profile ultimately enables this framework to yield less conservative estimates of the overall reliability of the candidate actuator architectures.

Figure 5.3 shows variation with missed detection rate for fixed MTBF and P_{FA}. As before, v3 is the least reliable and lies above the other curves. For low missed detection rates, v2 is the most reliable. For high missed detection rates, v4 is the most reliable. A trade-off that is similar to the one observed with servo MTBF is seen. For low missed detection rates, decoupled elevators (v2) is more reliable. For high missed detection rates, decoupled ailerons (v4) is more reliable.

Chapter 6

Conclusion

Small unmanned aircraft (UAVs) are increasingly finding new commercial applications. These applications require unmanned aircraft to be safely integrated into the national airspace. Safe integration of unmanned aircraft into the national airspace comes with several technical and regulatory challenges. Regulatory challenges are being addressed by policymakers in the government. Technical challenges are being addressed by the academia and the industry. One of the key technical challenges in UAV integration is assessing their reliability. Accurate reliability assessment is considered to be a significant step towards the certification of systems. Reliability assessment takes on additional significance because most small unmanned aircraft are not very reliable to start with. Hence, in addition to reliability assessment, there is a need to find design solutions that help increase unmanned aircraft reliability.

One of the key design parameters in the unmanned aircraft design process is the placement of actuators and aerodynamic control surfaces, collectively named "actuator architecture". Actuator architectures impact the overall aircraft reliability. This thesis introduced a general framework for assessing the reliability of these actuator architectures. Although the framework was presented for stuck control surface fault, it can be extended to other control surface fault modes. The framework treats control surface faults probabilistically. In doing so, the framework gives credit to the fact that not all faults have a binary cause-effect relationship with the overall system. In other words, some faults may cause degradation in system performance, but not lead to catastrophic failure of the aircraft. Such faults may be compensated for by using cross-functionality in other components.

The framework is described with the help of an example small UAV. Five different configurations of this example UAV are used to understand the relationship between actuator architectures and the overall reliability. Specifically, these five actuator architectures are different in the extent to which they exploit cross-functionality in their aerodynamic control surfaces. In applying the framework to the five candidate actuator architectures, several interesting and non-intuitive observations are made. For example, increasing the number of servos on a UAV does not necessarily increase its reliability. The overall reliability increases only if the additional servo has some level of cross-functionality with the other components. However, not all of these observations have simple explanations. In most cases, it is a complex interplay between servo reliability, actuator placement, surface coupling, and mission profile that governs the overall reliability.

Although primarily meant as an analysis tool, the framework that is presented in this thesis can also be used as a design tool. The primary objective during the UAV design process is typically performance and not reliability. However, this might change soon, given the increasing costs of operating and maintaining unreliable UAVs. It is reasoned that the proposed framework might be useful to unmanned aircraft designers, while considering reliability in the design process. The actuator architecture is a key design parameter in the design process. This framework provides a method by which UAV designers can quickly assess the reliability of candidate actuator architectures, before making a design decision. This framework marks a shift from the reliance on rules of thumb to a more analytically rigorous approach in making design decisions. The framework is considered useful despite the non-intuitive observations mentioned earlier. These non-intuitive observations are in themselves justifications for applying the more rigorous assessment methods, than relying on mere rules of thumb.

This framework marks an initial attempt at integrating the dynamics of the aircraft into the reliability assessment process. Several assumptions were made in this thesis. Future work will involve relaxing these assumptions and validating the analysis method.

References

[1] Frost & Sullivan. Study analysing the current activities in the field of uav. *EC Enterprise and Industry*, 2011.

[2] European Cmmsn. A new era for aviation opening the aviation market to the civil use of remotely piloted aircraft systems in a safe and sustainable manner. 2014.

[3] United States Congress. House resolution 658: FAA modernization and reform act of 2012, 2012. Section 332: Integration of Civil Unmanned Aircraft Systems into National Airspace System.

[4] Federal Aviation Administration. Notice of proposed rulemaking, February 2015.

[5] Y. C. Yeh. Triple-triple redundant 777 primary flight computer. In *Proceedings of the 1996 IEEE Aerospace Applications Conference*, pages 293–307, Aspen, CO, USA, 1996.

[6] University of Minnesota. Uav research group. `www.uav.aem.umn.edu`, 2014.

[7] J. Amos, E. Bergquist, J. Cole, J. Phillips, S. Reimann, and S. Shuster. Uav for reliability. `www.aem.umn.edu/~SeilerControl/SafetyCritical.shtml`, December 2013.

[8] B. Wu. *Reliability Analysis of Dynamic Systems: Efficient Probabilistic Methods and Aerospace Applications*. Elsevier, 2013.

[9] M. Hamada. *Bayesian Reliability*. Springer New York, 2008.

[10] P. Goupil. Oscillatory failure case detection in the A380 electrical flight control system by analytical redundancy. *Control Engineering Practice*, 18(9):1110 – 1119, 2010.

[11] A. M. Murch, Y. C. Paw, R. Pandita, Z. Li, and G. Balas. A low cost small uav flight research facility. In Florian Holzapfel and Stephan Theil, editors, *Advances in Aerospace Guidance, Navigation and Control*, pages 29–40. Springer-Verlag Berlin Heidelberg, 2011.

[12] A. Dorobantu, W. Johnson, F. A. Lie, B. Taylor, A. Murch, Y. C. Paw, D. Gebre-Egziabher, and G. Balas. An airborne experimental test platform: From theory to flight. In *American Control Conference*, pages 659–673, June 2013.

[13] F. A. Lie, A. Dorbantu, B. Taylor, D. Gebre-Egziabher, P. Seiler, and G. Balas. An airborne experimental test platform: From theory to flight (part 1). In *InsideGNSS*, pages 44–58, April 2014.

[14] J. Amos, E. Bergquist, J. Cole, J. Phillips, S. Reimann, and S. Shuster. Uav for reliability build. `www.aem.umn.edu/∼SeilerControl/SafetyCritical.shtml`, May 2014.

[15] B. L. Stevens and F. L. Lewis. *Aircraft Control and Simulation*. John Wiley & Sons, 1992.

[16] G. Hoe, D. Owens, and C. Denham. Forced oscillation wind tunnel testing for faser flight research aircraft. In *AIAA AFM Conference*, 2012.

[17] D. Owens, D. E. Cox, and E. A. Morelli. Development of a low-cost sub-scale aircraft for flight research: The faser project. In *25th AIAA Aerodynamic Measurement Technology and Ground Testing Conference*, 2006.

[18] Boeing Aerospace Company. Built-in-test verification techniques, 1987.

[19] S. X. Ding. *Model-Based Fault Diagnosis Techniques: Design Schemes, Algorithms, and Tools*. Springer-Verlag, Germany, first edition, 2008.

[20] R. C. Nelson. *Flight Stability and Automatic Control*. McGraw-Hill, 1998.

[21] M. V. Cook. *Flight Dynamics Principles*. Elsevier, second edition, 2007.

[22] N. H. McClamroch. *Steady Aircraft Flight and Performance*. Princeton University Press, 2011.

[23] J. E. Wilborn and J. V. Foster. Defining commercial transport loss-of-control: A quantitative approach. In *AIAA AFM Conference*, 2004.

[24] J. M. Urnes, E. Y. Reichenbach, and T. A. Smith. Dynamic flight envelope assessment and prediction. In *AIAA Guidance, Navigation and Control Conference and Exhibit*, Honolulu, HI, August 2008. AIAA.

[25] J. F. Murtha. An evidence theoretic approach to design of reliable low-cost uavs. Master's thesis, Virginia Polytechnic Institute and State University, 2009.

[26] Office of the Secretary of Defense. Unmanned aerial vehicle reliability study, 2003.

[27] Volz Servos GmbH. Endurance test da 22-30-4128, 2009.

[28] J. W. Rice and R. D. McCorkle. Digital flight control reliability - effects of redundancy level, architecture, and redundancy management technique. In *AIAA GNC Conference*, 1979.

Appendix A

Miscellaneous Flight Envelopes

This chapter presents some miscellaneous flight envelopes for the BALDR UAV and is an extension to the results presented in chapter 4.

A.1 Lateral-Directional Flight Envelope

Specifically, the lateral-directional steady flight envelopes for BALDR are presented in figures A.1 and A.2, in the $R/A \times \beta$ and $R/A \times \phi$ planes, respectively. Both these figures have been created for configuration v0. One should note that since a nonlinear aircraft model is being trimmed, the boundaries of the envelope are implicitly defined by the nonlinear dynamics. From figure A.1, it is seen that there is an almost linear relationship between angle of sideslip (β) and rudder deflection (R). Trim points exist for any stuck rudder fault in the range $[-25°, +25°]$. However, the stuck rudder fault is accompanied by some non-zero sideslip angle. As an example, consider positive stuck rudder faults, i.e. rudders stuck trailing edge left. This rudder deflection will cause the aircraft to yaw to the left and enter into a positive sideslip. The slope of the sideslip-to-rudder curve is approximately equal to one. Rudder deflections of *any* magnitude in $[-25°, +25°]$ can be tolerated, as long as sideslips can be tolerated.

On the other hand, there is an inverse relationship between β and aileron deflection. This is consistent with flight dynamics. For example, when a positive sideslip is being maintained, a negative rolling moment is generated because of the side force on the vertical stabilizer. In order to compensate for this negative rolling moment, the ailerons

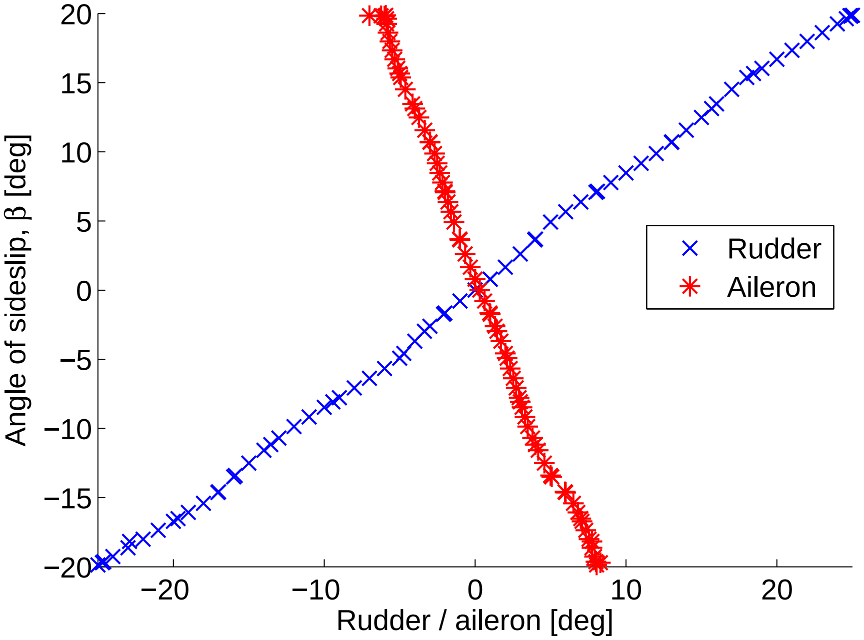

Figure A.1: Lateral-directional flight envelope in the $R/A \times \beta$ plane.

need to be deflected negatively, i.e. left aileron deflects trailing edge down. However, it is seen that trim points exist only for aileron deflections between $[-9°, +9°]$. Thus, aileron faults outside this range are not allowable according to the definitions in section 4.5. Note that figures A.1 and A.2, and the conclusions made above, are for configuration v0. Other configurations may allow for larger aileron faults to be tolerated. Aileron faults outside the range $[-9°, +9°]$ can be compensated if there are other aerodynamic surfaces that can provide rolling moment. For example, in configuration v2, the ailerons are coupled, but elevators are decoupled. Thus, in the event of a stuck aileron fault, elevators can provide compensative rolling moment, and larger aileron faults can be tolerated. This can clearly be seen in table 4.1. In table 4.1, the allowable stuck aileron range is $[-11°, +12°]$ for v2, as compared to $[-7°, +10°]$ for v3.

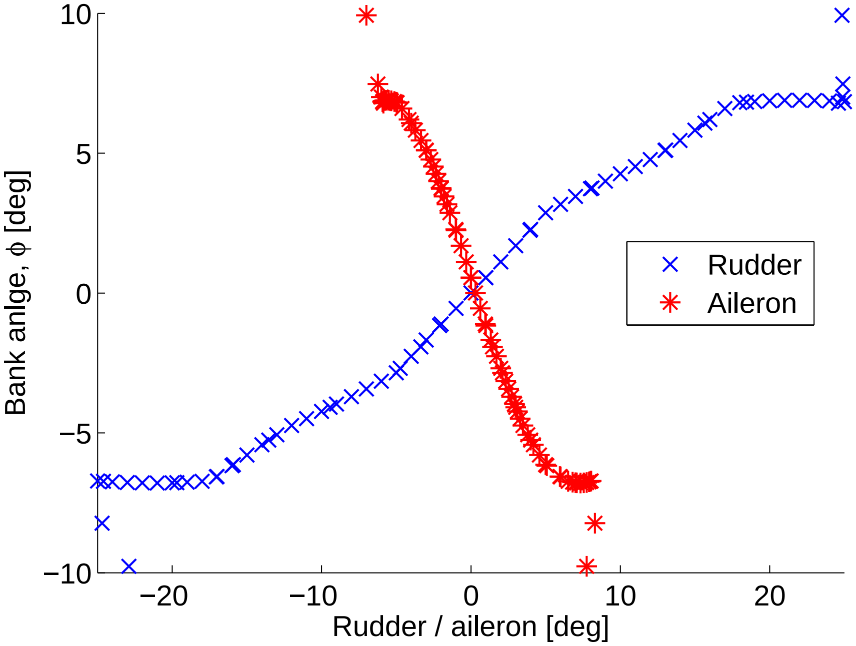

Figure A.2: Lateral-directional flight envelope in the $R/A \times \phi$ plane.

A.2 Throttle Effects on Longitudinal Flight Envelope

It was mentioned earlier in the thesis that throttle is not part of the reliability assessment process. It was reasoned that if there was an engine fault, the aircraft could glide to a safe landing. In order to provide some context to this assumption, the effect of throttle on the longitudinal flight envelope is presented in figure A.3. The motivation of this section is to understand the overall significance of throttle faults so that this fault mode may be included in the reliability analysis in the future. Figure A.3 shows the flight envelope in the $V \times \gamma$ plane.

Engine failures can have many causes, but the effect is often a reduction in, or total loss of, thrust. There are four well-defined boundaries in these two plots: low throttle, high throttle, stall, and high speed. In figure A.3, the low throttle boundary is the green curve. At the low throttle boundary, $\tau = 0$ and the throttle is closed. Indeed, for any fixed value of throttle, there is an inverse relationship between γ and V. Shallow glide slopes are possible only at low airspeeds. Conversely, steep glide slopes are possible only at high airspeeds. The specific case of straight & level flight is interesting to analyze.

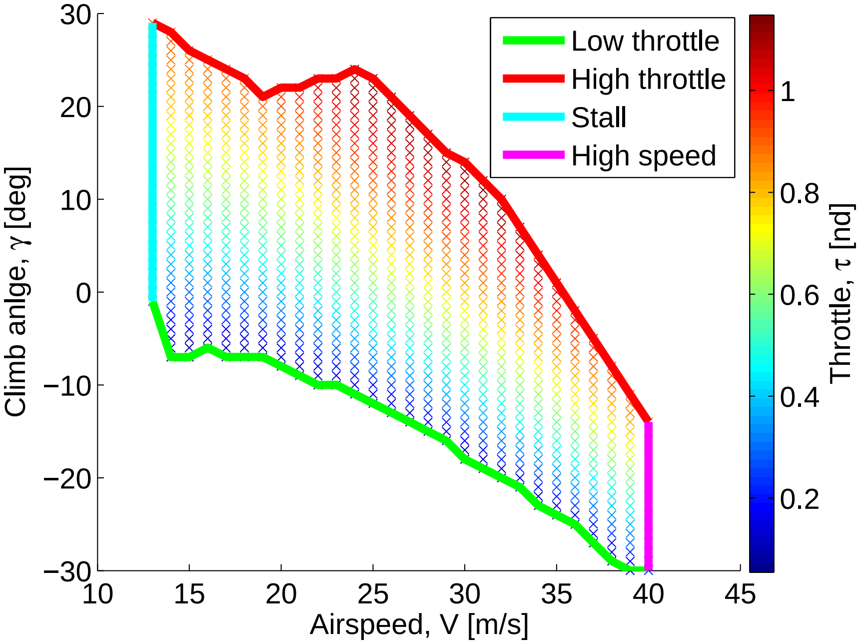

Figure A.3: Throttle effects on the longitudinal flight envelope in the $V \times \gamma$ plane.

For $\gamma = 0$ (level flight), lower throttle corresponds to lower airspeeds, and higher throttle corresponds to higher airspeeds. The high throttle limit is reached when the throttle is fully open.

From this plot, it is seen that throttle faults can be tolerated in the sense that steady descent trim points can be found. The glide slope during the steady descent phase can be controlled by controlling the airspeed (presumably using the elevator). This does not fit the allowable fault definition made in section 4.5, because straight & level trim points cannot be found. Future work will involve modifying the definition of the allowable fault so as to include throttle failures. Moreover, the current description of the minimal flight envelope is simplistic because the flight path that is generated after the onset of a fault is composed of piecewise steady modes. This description needs to be made more rigorous before additional fault modes are included in the analysis.